

Supplemental material for the Data Repository

Comeau et al., 2017, Electrical structure beneath the Hangai Dome, Mongolia: Magnetotelluric evidence for lithospheric melt and implications for uplift dynamics

DR1. Magnetotelluric data

Typical magnetotelluric (MT) data collected in the study area were high quality and had a very low noise level. Data were recording for an average of 5 days at broadband and telluric-only sites and for 16 days at long-period sites. A typical MT sounding from the study area is shown in **Figure DR1**, with apparent resistivity and phase curves for each impedance tensor component and real and imaginary parts for each tipper component (*e.g.*, Chave and Jones, 2012). The offset of the apparent resistivity curves is common in this dataset and is due to static shift effects, which are constant (on a log-scale), frequency-independent shifts of the curves caused by near-surface resistivity structure that occurs at a small spatial length scale (*e.g.*, Jones, 1988).

The survey area was separated into three regions: north of the Hangai Mountains (0 - 190 km along profile, measured from the northern-most site; including sites 2000 – 2190, roughly all north of Tsetserleg), across the Hangai Mountains (190 - 310 km; sites 2200 - 2330), and south of the Hangai Mountains (310 - 430 km; sites 2335 – 2430, roughly all south of Bayankhongor). For each site the sum of the squared elements of the impedance tensor (SSQ-average) and their geometric mean were calculated (Rung-Arunwan et al., 2016). The geometric mean represents a regional 1-D average and is believed to be free from a static shift. **Figure DR2** illustrates the consistency of the apparent resistivity and phase curves in the northern and central regions despite large (two orders of magnitude) static shift effects, but reveals some differences in the south.

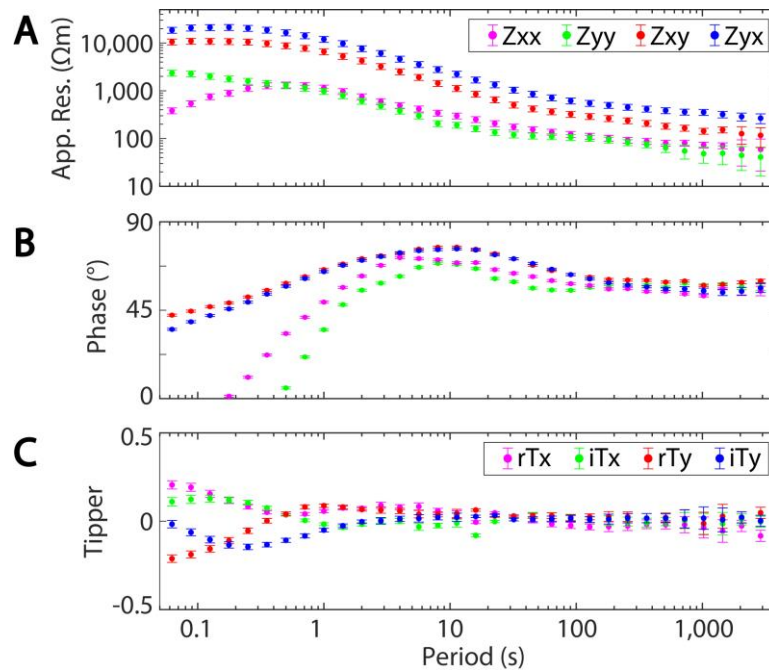


Figure DR1. A typical MT sounding from the study area. Apparent resistivity (A), phase (B), and tipper (C) data for MT site 2350.

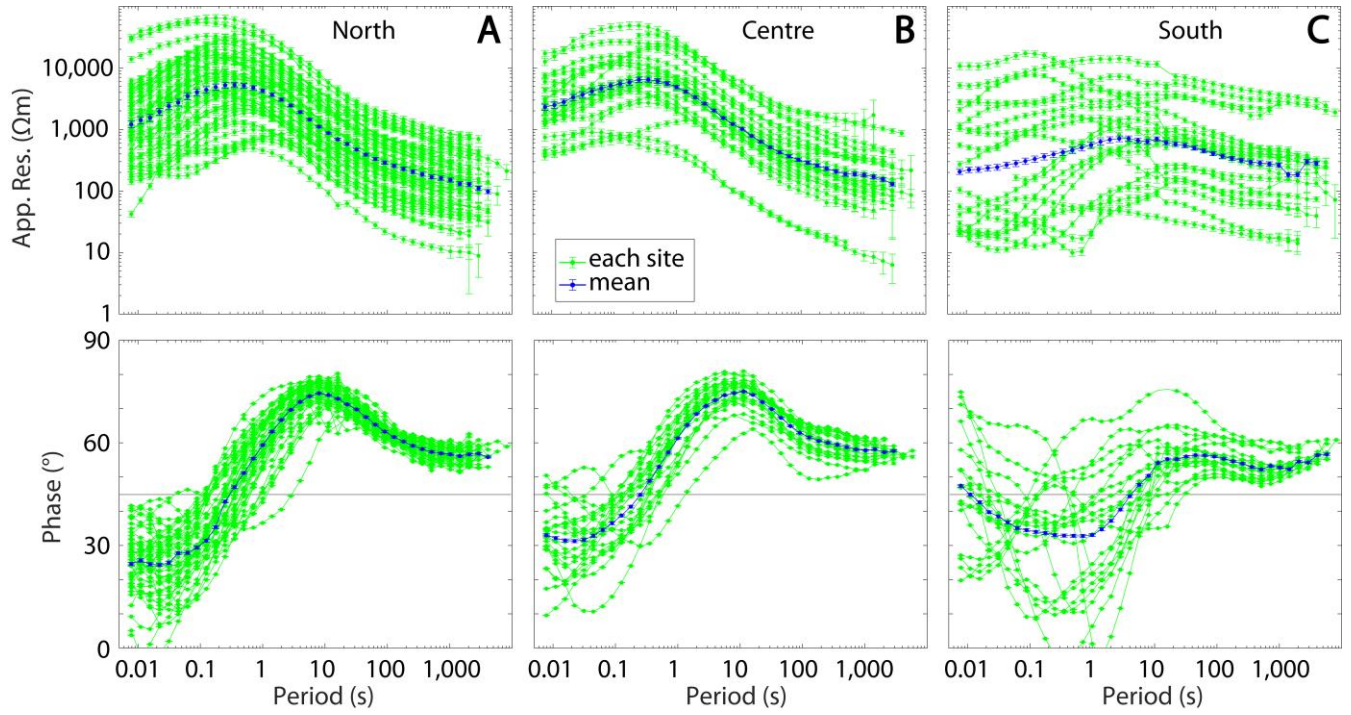


Figure DR2. Apparent resistivity and phase curves from the SSQ-average for individual sites (green lines) and their geometric mean (blue lines) from three regions: northern (A), central (B), and southern (C) Hangai. The offsets of the apparent resistivity curves, due to static shift effects, are evident. The northern and central regions are remarkably consistent, having similar-shaped apparent resistivity and phase curves, but the southern region is noticeably different.

DR2. Dimensionality analysis

Geo-electric strike direction

Dimensionality analysis determines if a 2-D or 3-D resistivity model is needed to interpret the measured MT data. For 2-D data, tensor decomposition can be used to estimate the geo-electric strike direction (e.g., [Groom and Bailey, 1989](#); [McNeice and Jones, 2001](#)). Tensor decomposition is implemented on a site-by-site basis, which allows for a different strike angle to be computed at each site. This is shown in [Figure DR3](#) in both map and rose diagram form. Phase tensor analysis was used to verify this result (e.g., [Caldwell et al., 2004](#); [Booker, 2014](#); see below). It should be noted that the strike directions determined have an inherent 90° ambiguity, but one direction must be chosen based on additional knowledge. Interestingly, the strike directions over the Hangai Mountains (central region) are more scattered and vary slightly from those observed in the southern and northern regions, indicating more complex structures.

The strike direction also varies for each frequency recorded. At short periods (<1 s), there is no well-defined strike direction because the electromagnetic signals are only sampling the near surface resistivity structure, which is approximately 1-D or is controlled by local structures. At longer periods (>1 s) the MT signals sample deeper in the Earth and a well-defined regional strike direction of N105°E can be observed. The strike angle is geologically plausible because it is approximately orogeny-parallel (N109°E - N119°E) and parallel to the main fault zones in the area (N118°E - N122°E). A consistent trend is observed with seismic anisotropy results that indicate a fast direction of N115°E - N134°E ([Barruol et al., 2008](#)).

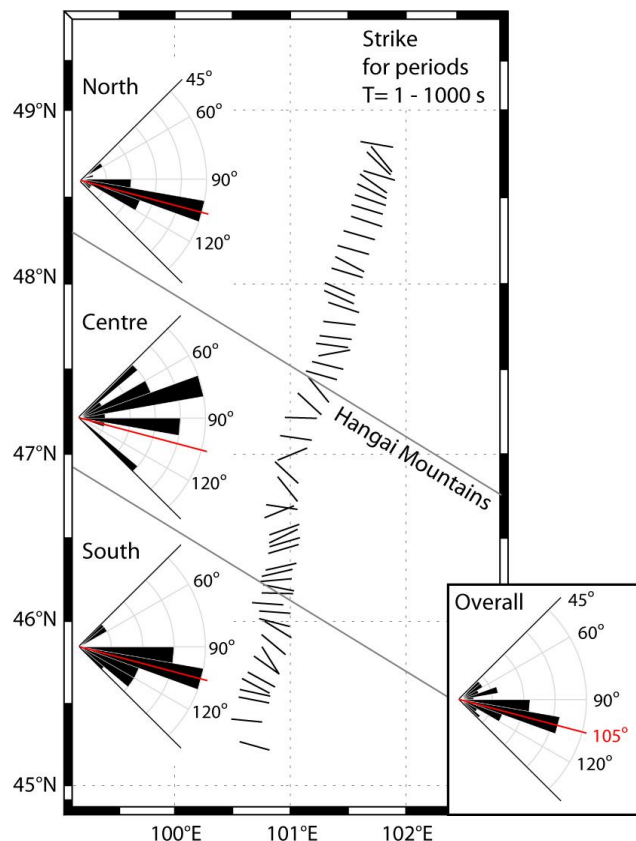


Figure DR3. Strike analysis results using the tensor decomposition method are presented in map view and as rose diagrams, for each region. A fairly consistent strike direction is seen over the whole Hangai region, although there is scatter in the central region, across the Hangai Mountains, indicating complex structure. Overall, a strike direction of N105°E (red line) fits most of the data.

Suitability of a unique geo-electric strike direction

A further analysis to determine if a unique strike direction is applicable to all MT sites is required if a 2-D inversion is to be undertaken. The strike direction is set to a given angle and the misfit for the tensor decomposition is determined for all sites and all periods. The misfit is calculated with a root mean squared (RMS) misfit between the 2-D MT impedance values predicted by the tensor decomposition method and the measured MT values, using an error floor of 3% (e.g., McNeice and Jones, 2001). Figure DR4A shows the results of this analysis as the strike direction is varied from N90°E to N180°E. A clear minimum misfit can be seen at a strike angle of N105°E. However this does not fully describe how well all the data is fit, thus Figure DR4B shows how the misfit varies along the profile for each period when the strike angle is set to the preferred direction of N105°E. The generally low misfit values (< 2) indicate that a 2-D approach is valid. Some areas with higher misfits (i.e., red colours) may be due to 3-D effects.

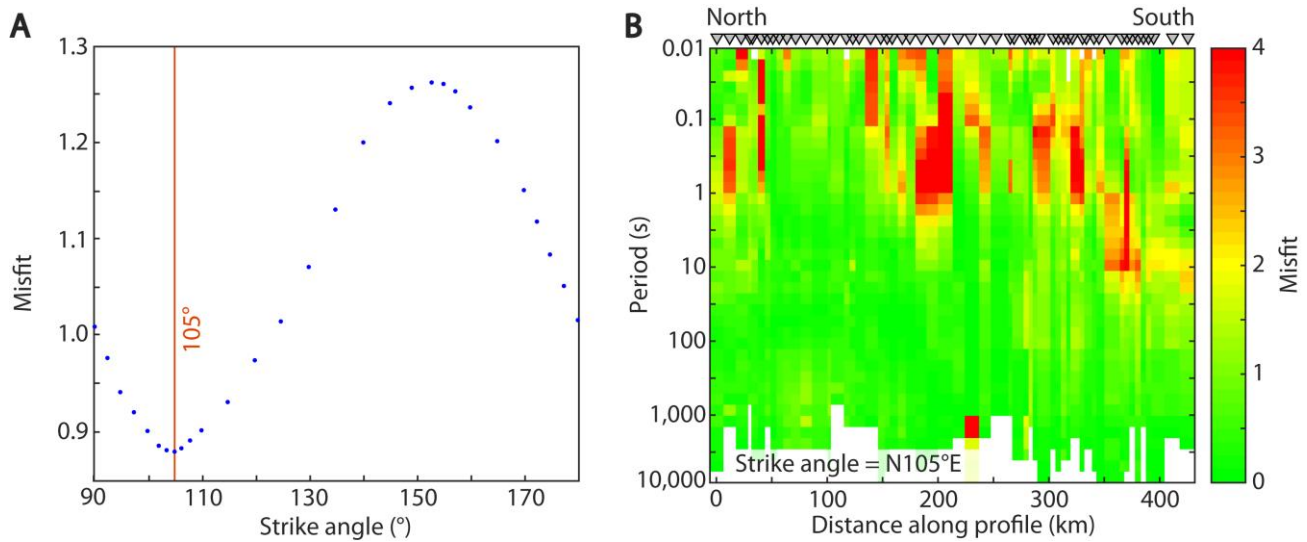


Figure DR4. A. Fit from the tensor decomposition method for various strike directions, measured clockwise from North. The minima shows the preferred strike direction. **B.** Pseudosection showing the fit from the tensor decomposition method when a strike direction of N105°E is used for all sites. This analysis is used to determine whether a single strike direction reasonably fits the data for all sites and all periods. Some areas (i.e., red colours) are distorted and may be better fit by a 3-D analysis.

Induction vectors analysis

Induction vectors are computed from the vertical magnetic fields generated by excess electric currents induced in the Earth and are sensitive to lateral changes in subsurface resistivity. Their orientation can help eliminate the ambiguity of strike directions inherent in the tensor decomposition and phase tensor methods. If the Earth has a 2-D resistivity structure the real components of the induction vectors will be orthogonal to the geo-electric strike direction and will point away from the edges of a conductor (Wiese convention; e.g., Wiese 1962; Berdichevsky and Dmitriev, 2008). The real components of the induction vectors are plotted in Figure DR5 for three representative periods. At short periods (e.g., 0.5 s, as in A) they are scattered, which can be expected because they are sensitive to shallow, local anomalies. At intermediate periods (e.g., 8 s, as in B) the induction vectors point away from a regional conductive zone located below the Hangai Mountains. Those located above the conductive zone will not be sensitive to it, but rather to the small variations within it, and will therefore appear small and scattered. The large amplitude vectors at the southern end of the profile clearly define the southern edge of the major conductor. The longer period data (e.g., 128 s, as in C) are consistent, but are more affected by noise and are smaller in amplitude and more scattered.

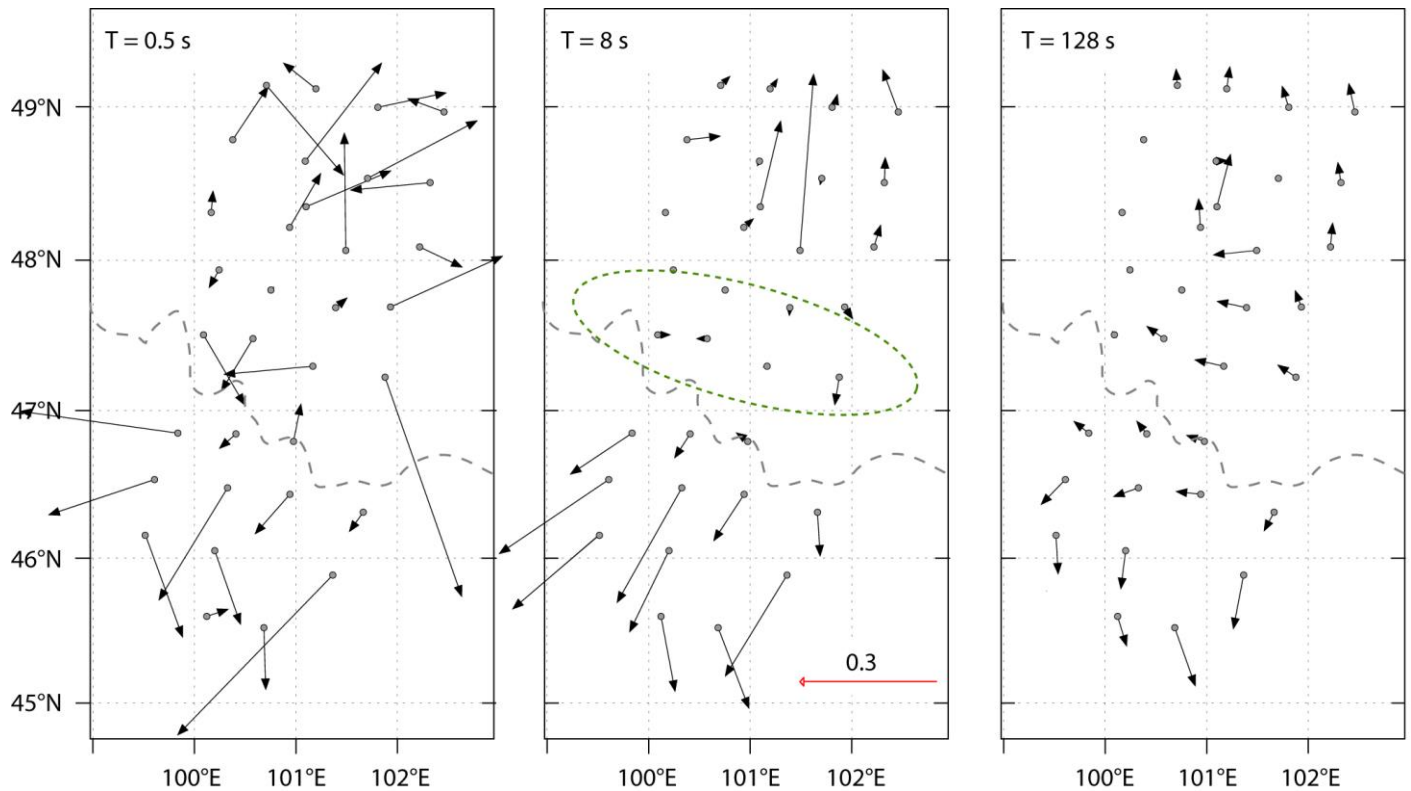


Figure DR5. Real induction vectors at various periods ($T = 0.5, 8, 128$ s) are plotted in map view using the Wiese convention. In a 2-D environment they should point away from conductive bodies and be perpendicular to the geo-electric strike direction. A scale arrow (amplitude 0.3; red) is provided for reference. The dotted green oval indicates a hypothetical conductive zone below the Hangai Mountains that the induction arrows are pointing away from. Dashed grey line is the divide of the Hangai Mountains.

Phase tensor analysis

The phase tensor method (Caldwell et al., 2004; Bibby et al., 2005) can give information on dimensionality (and geo-electric strike direction) without imposing a priori the condition of two-dimensionality. Furthermore, the phase tensor is not affected by galvanic distortions (e.g., static shift). The phase tensors can be plotted in pseudo-section view as ellipses and coloured with their phase-tensor skew value (ψ ; Booker, 2014), as in Figure DR6. They will appear as a circle for a 1-D Earth environment and as an ellipse for a 2-D or 3-D Earth environment. Skew values for a perfect 2-D Earth should be equal to 0° (blue colours). Skew values above $\sim 6^\circ$ (yellow to red colours) indicate that the diagonal values of the MT impedance tensor are within an order of magnitude of the off-diagonal values, thus indicate that distortion and/or 3-D effects are significant.

In summary, the dimensionality analysis above establishes that a 2-D assumption is valid for this profile as a whole. However, it is clear that certain regions of the profile do display distortion and/or local 3-D resistivity structure, specifically the central region of the profile and the southern portion of the profile. These 3-D aspects would be better understood with a full 3-D model, and future work will proceed in this direction.

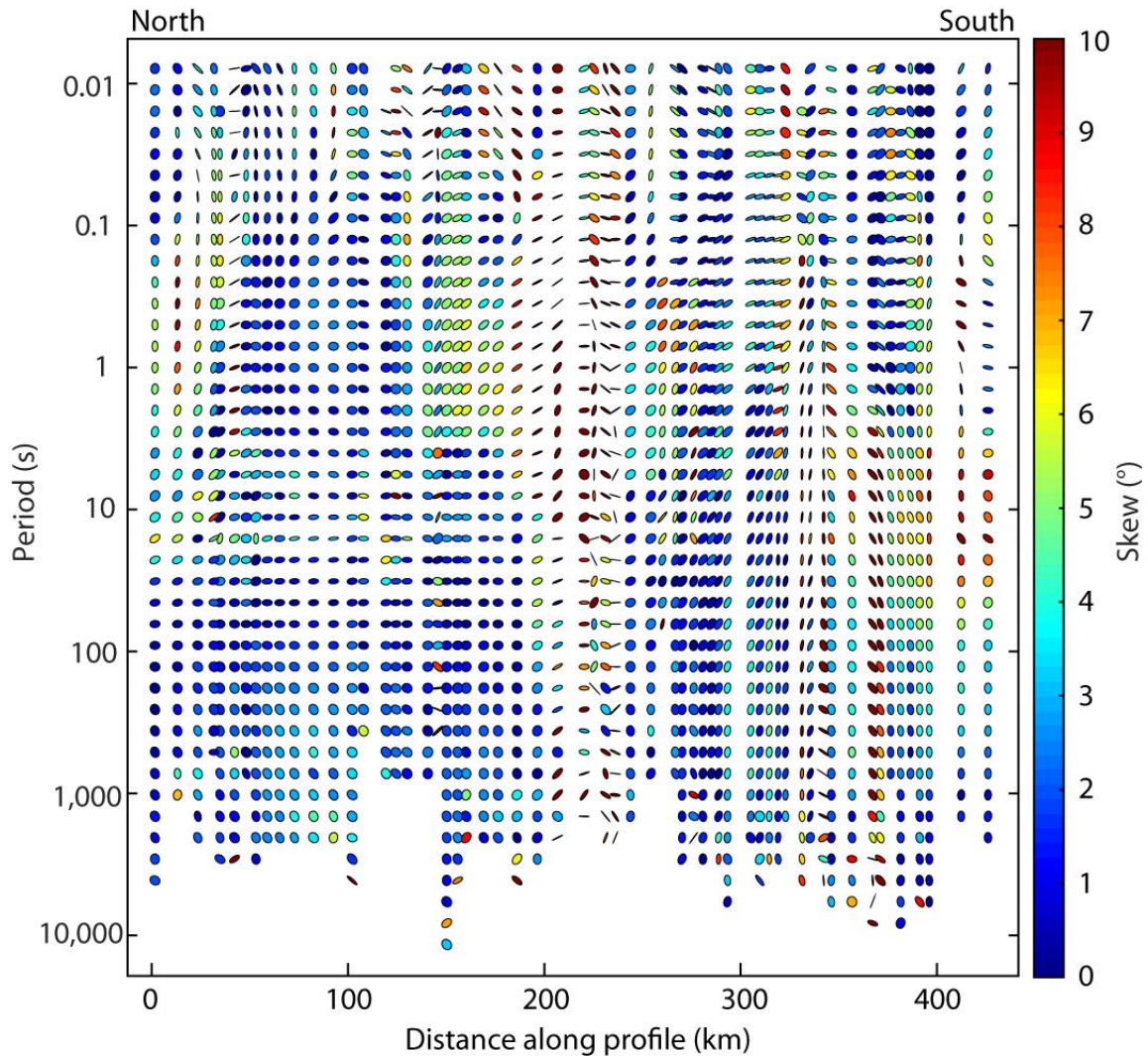


Figure DR6. Phase tensor ellipses for all periods and all sites plotted along the profile and coloured with their skew values. High skew values (yellow to red colours) indicate significant distortion and/or 3-D effects.

DR3. Inversion of magnetotelluric data

1-D Inversion

To begin, 1-D models were produced by inverting the geometric mean of the SSQ-average computed from the MT data (blue lines in Figure DR2). The 1-D inversion code used was based on a probabilistic algorithm that samples a number of probable (i.e., low RMS-misfit) models to quantify the uncertainty of the solution (Grayver and Kuvshinov, 2016) was. A probability density function (PDF) is calculated from the distribution of many models and is plotted with the best-fit-model in Figure DR7.

These models help illustrate the differences between the three regions and the uncertainty within each region. All regions show a near-surface conductor (C1) underlain by a resistive zone (R1). The northern and central regions clearly show a lower-crustal conductor (C2), which is underlain by weakly resistive zone (R2). These features are entirely absent from the southern region. A deeper conductive zone (C3) is detected at upper mantle depths in the northern and central regions. This feature is absent or very weak in the southern region. Additionally, these models highlight the reduced resolution within the deeper parts of the model (150 – 200 km depth) due to attenuation of the electromagnetic signals.

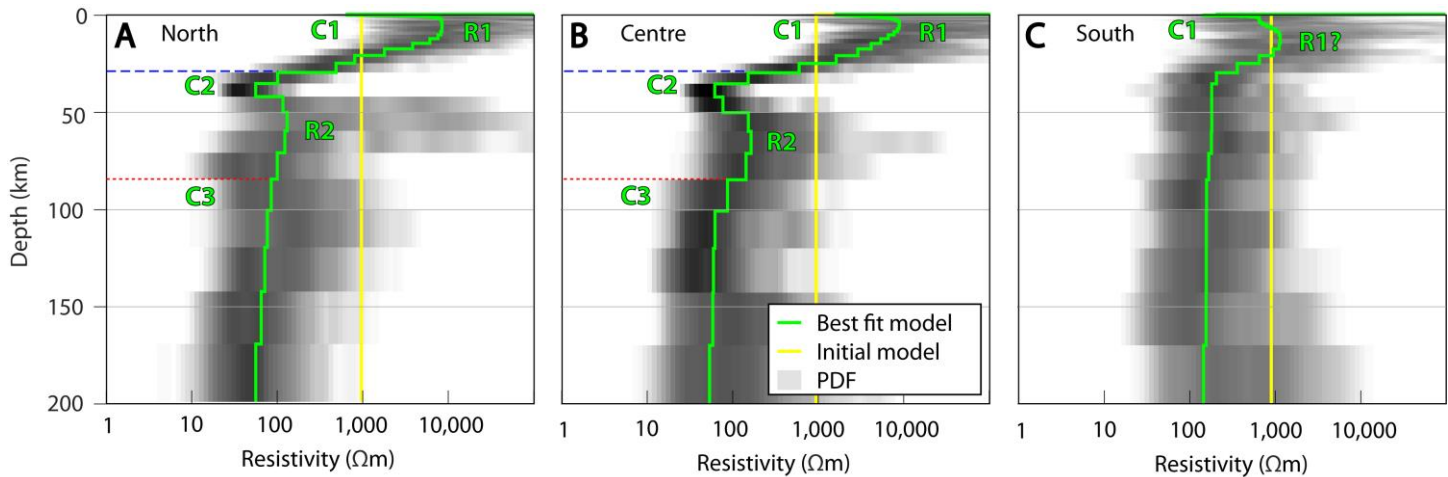


Figure DR7. The 1-D inversion models for each region of the Hangai area. Green line indicates the best fit model and the grey colour represents the probability distribution function (PDF) for multiple low-misfit models. Blue dashed line (30 km) and red dotted line (85 km) indicate depths where the resistivity drops below 100 Ωm . Note the distinctly different pattern in the southern region (C).

2-D Inversion

The dimensionality analysis performed above suggests that a 2-D inversion is valid for these MT data. First, the data were rotated to a strike direction of N105°E, as determined above, and the profile A-A' was created perpendicular to this direction. A joint 2-D inversion of TE-mode and TM-mode MT data (from electric currents flowing along strike, perpendicular to profile, and from currents flowing across strike, parallel to profile, respectively) was carried out using the EMILIA inversion algorithm (Kalscheuer et al., 2010), which is based on an Occam approach (Constable et al., 1987). No topography was included in the model, and thus depths are given below surface. An error floor of 5% (1.43°) was used for both TE-mode and TM-mode phase components, causing the inversion algorithm to closely fit these data, and an error floor of 10% was used for the TM-mode apparent resistivity. A high error floor of 100% was used on the TE-mode apparent resistivity in order to reduce the influence of the static shift effect (e.g., Jones, 1988). The inversion began with a 1,000 Ωm halfspace.

The 2-D inversion was repeated for a wide range of model regularization parameters, using a gradient model penalty, and an appropriate regularization parameter was chosen as a compromise between closely fitting the measured MT data and producing a spatially smooth model (e.g., deGroot-Hedlin and Constable, 1990). The inversion algorithm, using a damped approach (Kalscheuer et al., 2010), smoothly converged after 12 iterations, with the total RMS misfit reduced from 12.54 to 2.51. The total misfit is significantly influenced by the high frequency data because the variable near-surface layer is difficult to fit uniformly between sites. The TE-mode data also act to increase the total misfit, for example the RMS misfit of the TM-mode data alone is < 2.0 . The total RMS misfit at each site is plotted in Figure DR8 and a representative fit of the model to the MT data at several sites can be seen in Figure DR9. Pseudosections of measured MT data, modeled MT data, and their error-normalized residuals illustrate the close fit of the final 2-D model (see Figure DR10).

Testing the 2-D model's features

Many combinations of inversion parameters were thoroughly investigated, and the final model generated (presented in Figure 2) is representative of most cases. Variations in the strike direction, error floors, and starting models were all tested and little change in the broad model properties was observed. For example, the geo-electric strike angle was varied by $\pm 10^\circ$ and the starting model was varied from a halfspace of 1,000 Ωm to a layered 1-D model with no significant changes in the model's main features. Model resolution and sensitivity were investigated systematically using synthetic inversions.

The sensitivity and robustness of model features were tested in several ways, including by removing them from the model and comparing the data fit. When this was done the misfit increased, indicating a worse fit to the MT data without these features. The inversion was also re-started to test if the features were re-introduced, as they should be if they are required. It was observed that they were re-introduced, in order to better fit the MT data. These tests proved that the model's main features are all required. Crustal features are particularly well-constrained. However, these tests showed that the depth to the top boundary of the upper mantle conductor C3 below the northern region of the profile is not well-constrained and can vary. This is explained by the decrease in resolution and sensitivity below the crustal conductor and at depths greater than 150 km. Additionally, the geometry of C3 below the central Hangai is not well-constrained, and the data can be equally-well fit (difference in RMS misfit $< 3\%$) by a slightly narrower anomaly or by a wider, bulging anomaly, at the same location. None of these variations affect the interpretation of the model.

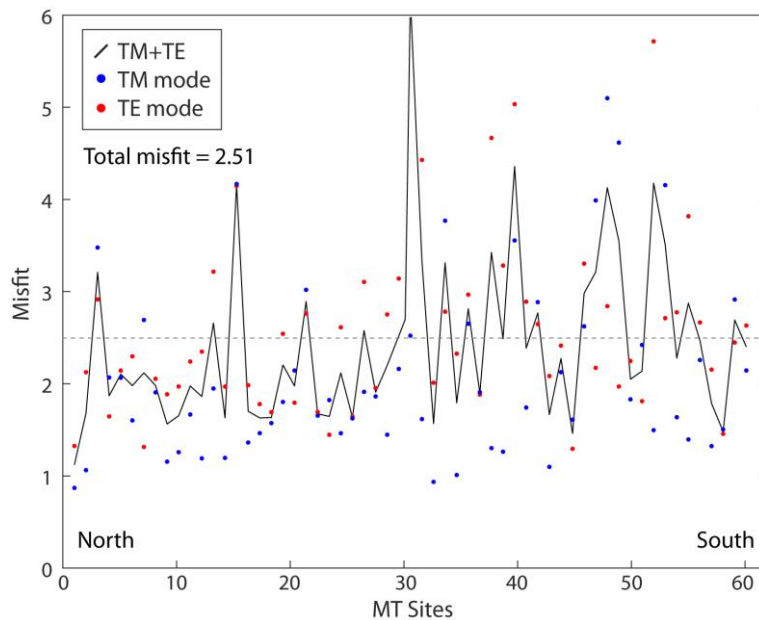


Figure DR8. Misfit for each site of the 2-D resistivity model. A misfit of 1.0 implies that the model fits within the specified error (see above). Misfits are higher for the southern region of the profile. The model has a total misfit of 2.51 (dashed line).

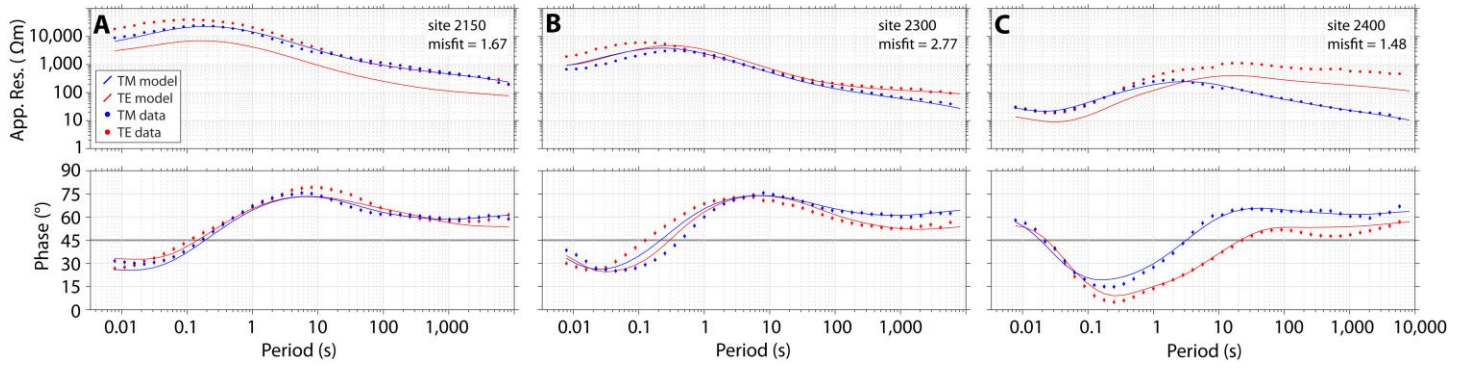


Figure DR9. Typical data fit for the resistivity model at several representative sites from the northern region (A), the central region (B), and the southern region (C). The site in A shows a static shift effect which has been corrected by the inversion algorithm, with little negative effect on the misfit. The site in B illustrates the difficulty in fitting the short-period data (<1 s), which increases the overall misfit, but that a high misfit (2.77 in this case) can still visually fit the data. The site in C demonstrates the distinctly different data seen in the southern region.

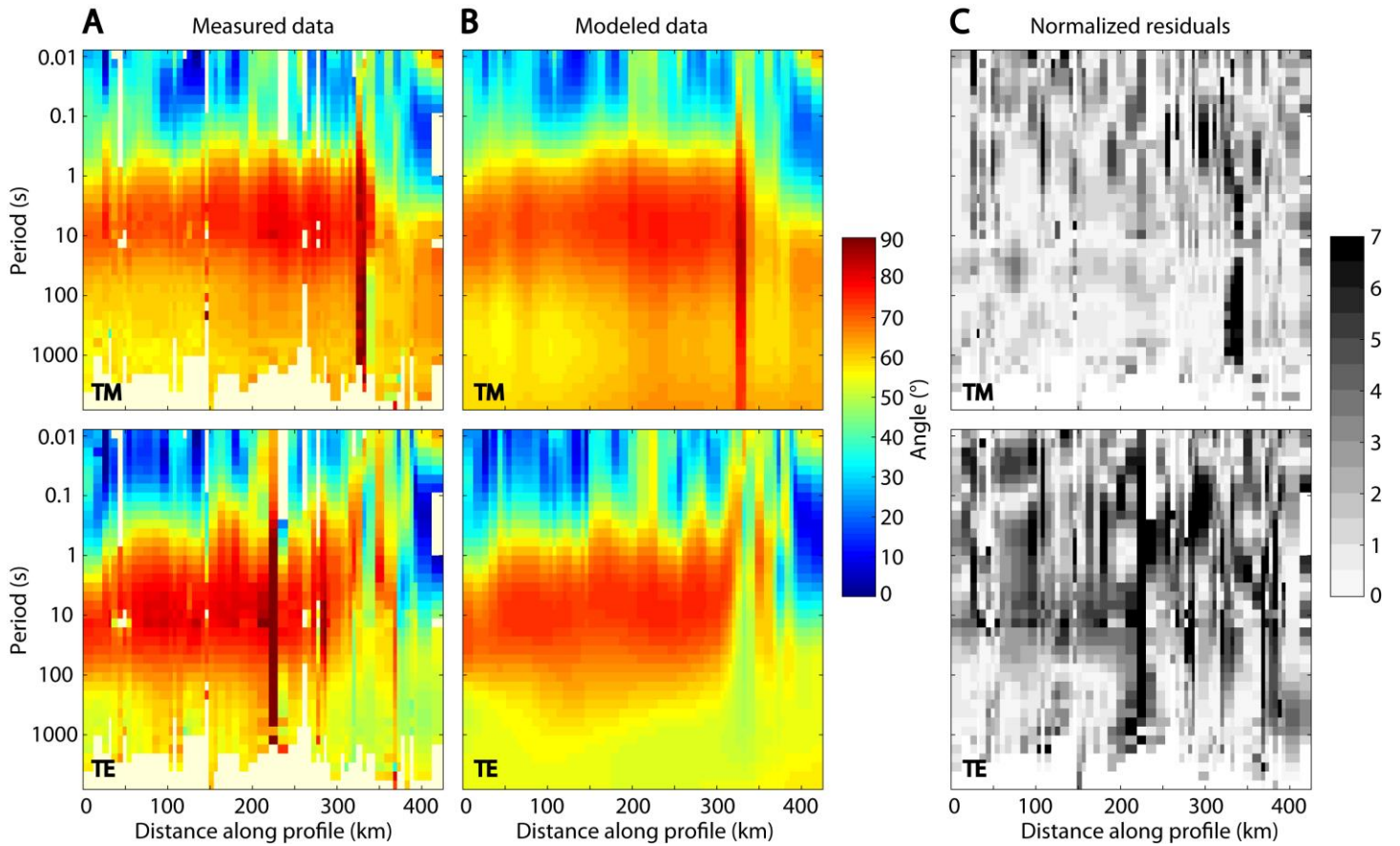


Figure DR10. Pseudosections of the impedance phase from the measured MT data (A) and the modeled data (B), for TM-mode (top row) and TE-mode (bottom row). Error-normalized-residuals (C), equivalent to the RMS misfit, illustrate that the data fit is generally good. The total model RMS misfit was 2.51.

DR5. Using MT data to determine melt fraction

Estimating melt resistivity

If the low-resistivity anomalies detected are due to partial melt alone we can determine the minimum required fraction of melt, following the approach of [Comeau et al. \(2016\)](#). Pure melt resistivity is controlled by the melt silica content, sodium content, water content, the pressure, and the temperature (e.g., [Nesbitt, 1993](#); [Nover, 2005](#); [Pommier and Le Trong, 2011](#)). With accurate geochemical and thermobarometry estimates it can be calculated with the SIGMELTS algorithm of [Pommier and Le Trong \(2011\)](#).

An average silica content of 50 weight percent (wt%; range of 44 – 54 wt%) and an average sodium content of 4 wt% (range of 2.5 – 5.5 wt%) are measured from collected lava samples ([Barry et al, 2003](#); [Hunt et al., 2012](#)). A range of water contents from 2 – 9 wt% are used in this study because high water contents for deep melts are feasible and do not exceed solubility limits ([Laumonier et al, 2016](#); [Laumonier et al, 2014](#); [Newman and Lowenstern, 2002](#)). Furthermore, using maximal conductivity values in the analysis allows us to calculate a true minimum required melt fraction.

Thermobarometry estimates from garnet and xenolith samples give temperatures of 1070 - 1200 °C for depths of 60 – 80 km ([Barruol et al., 2008](#); [Barry et al, 2003](#); [Harris et al., 2010](#)) and 800 - 880 °C for depths of 30 – 45 km ([Barruol et al., 2008](#); [Ionov, 2002](#); [Ancuta et al., 2015](#)). The pressure is calculated from the depth, assuming a simple lithostatic relation (i.e., $\text{pressure} = \text{density} \cdot \text{depth} \cdot g$, $g = 9.81 \text{ m/s}^2$). The pure melt resistivity is predicted for a range of compositions, pressures, and temperatures ([Figure DR11](#)). The analysis predicts a pure melt resistivity of $\sim 0.8 \Omega\text{m}$ (conductivity = 1.23 S/m) for a depth of ~ 30 km and $\sim 1.4 \Omega\text{m}$ (0.73 S/m) for a depth of ~ 70 km.

Melt fraction calculation

A suitable two-phase equation to combine the resistivity of the pure melt and the rock matrix is needed. This study uses both the modified Archie's law (MAL) of [Glover et al. \(2000\)](#) and the Hashin-Shtrikman lower bound from [Hashin and Shtrikman \(1963\)](#), because they allow electrical conduction through the rock matrix, which becomes significant at high temperatures. The resistivity of the rock matrix was computed using the resistivity-temperature relation of [Hashim et al. \(2013\)](#). The melt geometry can be highly interconnected, modeled by using a cementation factor of $m = 1.0$ in Archie's law, or the melt may be located in isolated pores, using $m = 2.0$ ([Glover et al., 2000](#)). The Hashin-Shtrikman lower bound realistically represents normal interconnection for lithospheric melts ([ten Grotenhuis et al., 2005](#); [Unsworth and Rondenay, 2012](#)). When the pure melt resistivity estimates above are combined with the rock matrix resistivity a minimum melt fraction to explain any observed bulk resistivity can be estimated ([Figure DR12](#)). If higher values of pure melt resistivity are used then a higher melt fraction is required. Therefore these values represent the minimum melt fractions required by the MT data.

The conductive anomaly observed in the resistivity model has a resistivity of $\sim 30 \Omega\text{m}$, and is located at ~ 30 km depth (C2), therefore a minimum melt fraction of 2 - 5% is required (computed from the range of allowed temperatures, see above). A similar anomaly at a depth of ~ 70 km (C3) needs a minimum melt fraction of 4 - 8% to explain the observed MT data. For water under-saturated conditions (i.e., a low water content of 3%) this values increases, and a minimum melt fraction of 8 - 18% and 5 - 10% and is required for the shallow case and the deep case. The water content has a small effect on the deeper anomaly but significantly increases the melt fraction required for the crustal anomaly. For a more isolated melt geometry (using Modified Archie's Law with cementation exponent $m = 1.5$) a minimum melt fraction of 7 - 11% and 9 - 14% is required, for the shallow and deep cases respectively. This is approximately double the amount as for the interconnected case. Saline aqueous fluids, which can be much lower resistivity than melt, in addition to melt or alone could also explain the observed low-resistivity values.

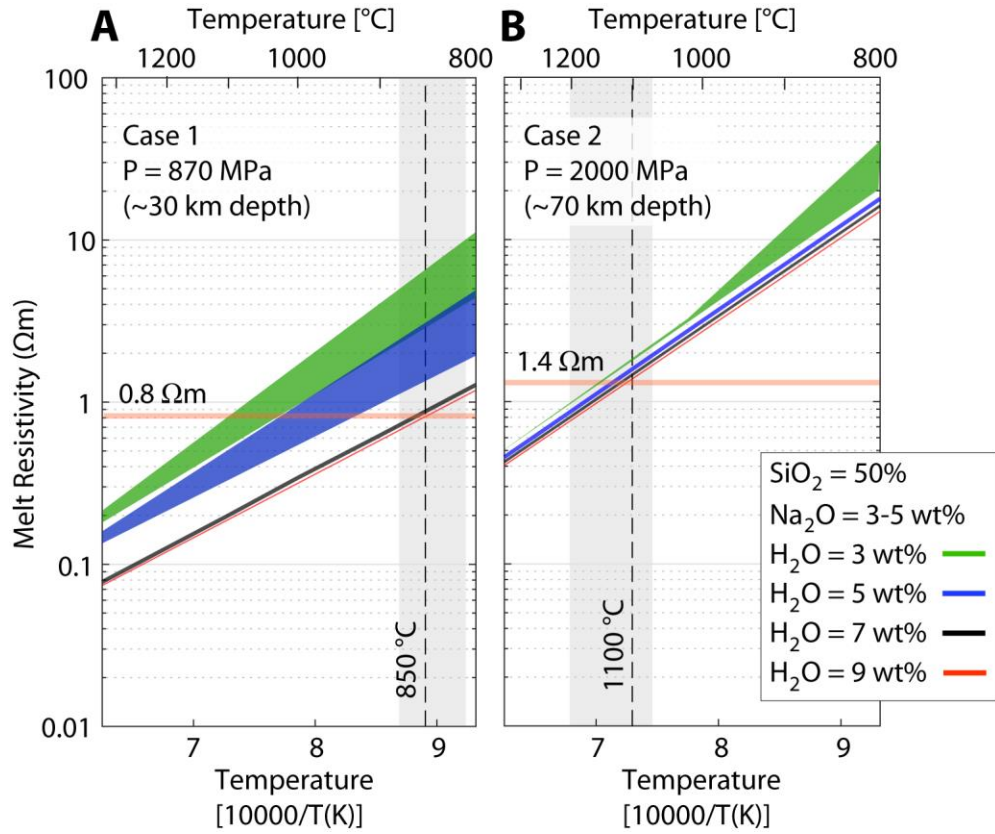


Figure DR11. Variation of pure melt resistivity as a function of temperature for melts at ~30 km depth (A; case 1) and ~70 km depth (B; case 2) for a range of water and sodium contents. The resistivity data were computed using the SIGMELTS algorithm of [Pommier and Le Trong \(2011\)](#). The temperature estimates from thermobarometry of Hangai lavas are shown in grey, with the temperature used in the calculations indicated with a dashed line. Pure melt resistivities of $\sim 0.8 \Omega\text{m}$ and $\sim 1.4 \Omega\text{m}$ were found for case 1 and 2, respectively.

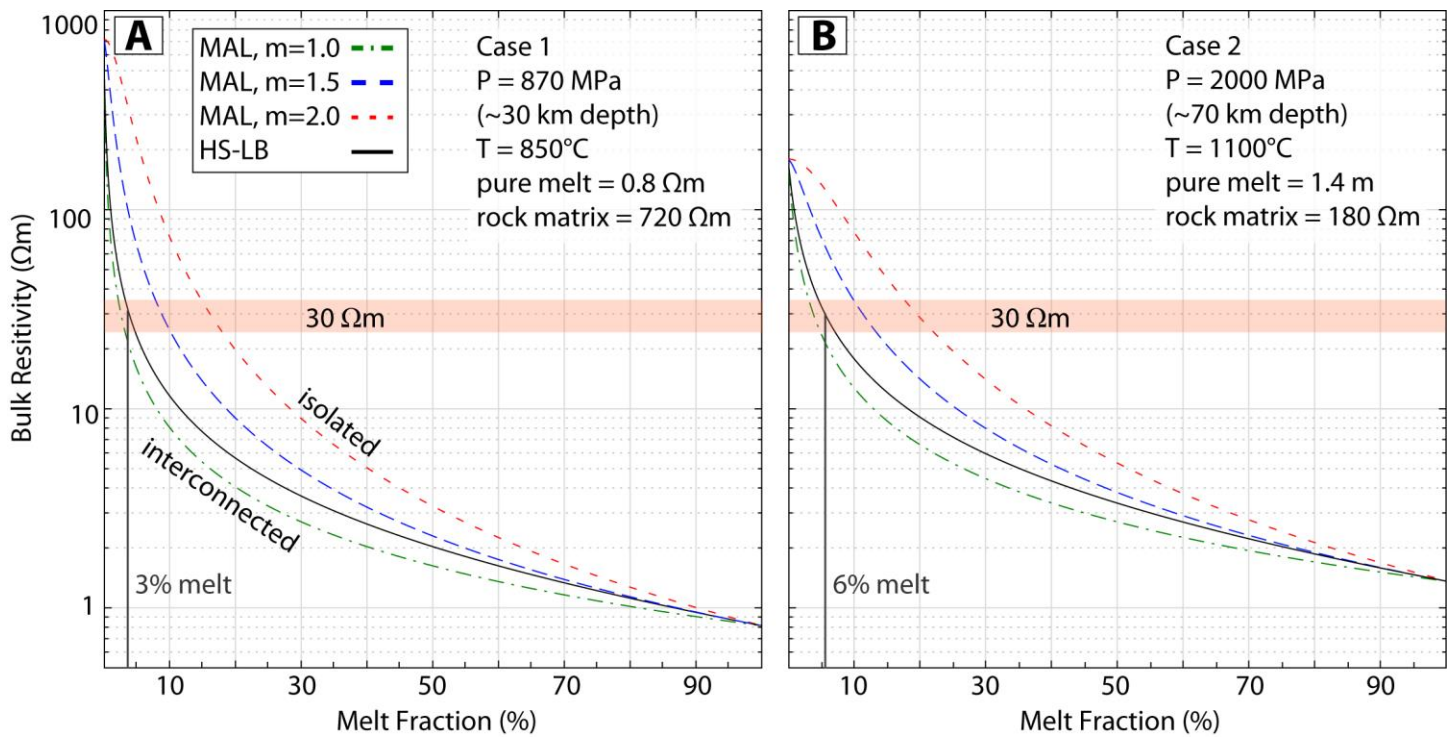


Figure DR12. Bulk resistivity of a partially molten rock as a function of melt fraction for two cases (A and B), as in Figure DR11. Dashed lines show the bulk resistivity computed using the modified Archie's law (MAL; Glover et al., 2000) for various degrees of melt interconnection, from very well-connected ($m=1.0$) to isolated ($m=2.0$), see text for details. The black line shows the Hashin-Shtrikman lower bound (HS-LB; Hashin and Shtrikman, 1963), which is the preferred value for interconnected lithospheric melts. The approximate resistivity of the anomalies C2 and C3 is $\sim 30 \Omega\text{m}$, and this intersection gives a minimum bound on the melt fraction required to fit the MT data. If higher values of pure melt resistivity are used then a higher melt fraction is required.

DR6. Additional References

- Ancuta, L.D., Carlson, R., Ionov, D.A., 2015, Geochronology and Geochemistry of Lower Crustal Xenoliths: Exploring the Formation of the Lower Crust Beneath Central Mongolia: Abstract #V51C-3044 presented at 2015 Fall Meeting, American Geophysical Union, San Francisco, USA.
- Berdichevsky, M.N., and Dmitriev, V.I., 2008, Models and Methods of Magnetotellurics: Springer-Verlag, Berlin, 564 p.
- Bibby, H.M., Caldwell, T.G., Brown, C., 2005, Determinable and non-determinable parameters of galvanic distortion in magnetotellurics: Geophysical Journal International, v. 163, p. 915–930.
- Booker, J., 2014, The Magnetotelluric Phase Tensor: A Critical Review: Surveys in Geophysics, v. 35, p. 7-40.

- Caldwell, T.G., Bibby, H.M., Brown, C., 2004, The magnetotelluric phase tensor: *Geophysical Journal International*, v. 158, p. 457–469.
- Constable, S.C., Parker, R.L., Constable C.G., 1987, Occam's inversion - A practical algorithm for generating smooth models from electromagnetic sounding data: *Geophysics*, v. 52(03), p. 289–300.
- deGroot-Hedlin, C., and Constable, S., 1990, Occam's inversion to generate smooth two-dimensional models from magnetotelluric data: *Geophysics*, v. 55(12), p. 1613–1624.
- Glover, P., Hole, M.J., Pous, J., 2000, A modified Archie's Law for two conducting phases: *Earth and Planetary Science Letters*, v. 180, p. 369–383.
- Grayver, A.V., Kuvshinov, A.V., 2016, Exploring equivalence domain in nonlinear inverse problems using Covariance Matrix Adaption Evolution Strategy (CMAES) and random sampling: *Geophysics Journal International*, v. 205, p. 971–987.
- Groom, R., and Bailey, R., 1989, Decomposition of Magnetotelluric Impedance Tensors in the Presence of Local Three-Dimensional Galvanic Distortion: *Journal of Geophysical Research*, v. 94, p. 1913–1925.
- Hashim, L., Gaillard, F., Champallier, R., Le Breton, N., Arbaret, L., Scailie, B., 2013, Experimental assessment of the relationships between electrical resistivity, crustal melting and strain localization beneath the Himalayan-Tibetan Belt: *Earth and Planetary Science Letters*, v. 373, p. 20–30.
- Hashin, Z., and Shtrikman, S., 1962, A variational approach to the elastic behavior of multiphase minerals: *Journal of the Mechanics and Physics of Solids*, v. 11, p. 127–140.
- Jones, A., 1988, Static shift of MT data and its removal in a sedimentary basin environment: *Geophysics*, v. 53, p. 967–978.
- Laumonier, M., Gaillard, F., Muir, D., Blundy, J., Unsworth, M., 2016, Giant magmatic water reservoirs at mid-crustal depth inferred from electrical conductivity and the growth of the continental crust: *Earth and Planetary Science Letters*, v. 457, p. 173–180.
- Laumonier, M., Gaillard, F., Sifre, D., 2014, The effect of pressure and water concentration on the electrical conductivity of dacitic melts: Implication for magnetotelluric imaging in subduction areas: *Chemical Geology*, v. 418, p. 66–76.
- McNeice, G.W. and Jones, A.G., 2001, Multisite, multifrequency tensor decomposition of magnetotelluric data: *Geophysics*, v. 66, p. 158–173.
- Nesbitt, B.E., 1993, Electrical resistivities of crustal fluids: *Journal of Geophysical Research*, v. 98, p. 4301–4310.
- Newman, S., and Lowenstern, J.B., 2002, VolatileCalc: a silicate melt–H₂O–CO₂ solution model written in Visual Basic for Excel: *Computers and Geoscience*, v. 28, p. 597–604.
- Nover, G., 2005, Electrical properties of crustal and mantle rocks—A review of laboratory measurements and their explanation: *Surveys in Geophysics*, v. 26, p. 593–651.
- Rung-Arunwan, T., Siripunvaraporn, W., Utada, H., 2016, On the Berdichevsky average: *Physics of the Earth and Planetary Interiors*, v. 253, p. 1–4.
- ten Grotenhuis, S.M., Drury, M.R., Spiers, C.J., Peach, C.J., 2005, Melt distribution in olivine rocks based on electrical conductivity measurements: *Journal of Geophysical Research*, v. 110 (B12201), p. 1–11.

Wiese, H., 1962, Geomagnetische Tiefentellurik Teil II: Die Streichrichtung der Untergrundstrukturen des elektrischen Widerstandes, erschlossen aus geomagnetischen Variationen: *Geofisica pura e applica*, v. 52(1), p. 83–103.